Planck intermediate results VI : The dynamical structure of PLCKG214.6+37.0, a Planck discovered triple system of galaxy clusters

Ade, P. A. R.

2013-02-01

Ade , P A R , Juvela , M , Keihänen , E , Kurki-Suonio , H , Lähteenmäki , A , Poutanen , T , Suur-Uski , A -S , Tuovinen , J & Planck Collaboration 2013 , ' Planck intermediate results VI : The dynamical structure of PLCKG214.6+37.0, a Planck discovered triple system of galaxy clusters ' , Astronomy & Astrophysics , vol. 550 , pp. A132 . https://doi.org/10.1051/0004-6361/201220039

http://hdl.handle.net/10138/233699
https://doi.org/10.1051/0004-6361/201220039

other
publishedVersion

A&A 550, A132 (2013)
DOI: 10.1051/0004-6361/201220039

Astronomy & Astrophysics

Planck intermediate results

VI. The dynamical structure of PLCKG214.6+37.0, a *Planck* discovered triple system of galaxy clusters

Planck Collaboration: P. A. R. Ade[88], N. Aghanim[60], M. Arnaud[75], M. Ashdown[72,7], F. Atrio-Barandela[20], J. Aumont[60], C. Baccigalupi[87], A. Balbi[38], A. J. Banday[97,10], R. B. Barreiro[68], J. G. Bartlett[1,69], E. Battaner[99], K. Benabed[61,95], A. Benoît[58], J.-P. Bernard[10], M. Bersanelli[36,52], R. Bhatia[8], I. Bikmaev[22,3], H. Böhringer[81], A. Bonaldi[70], J. R. Bond[9], J. Borrill[15,91], F. R. Bouchet[61,95], H. Bourdin[38], R. Burenin[89], C. Burigana[51,34], P. Cabella[39], J.-F. Cardoso[76,1,61], G. Castex[1], A. Catalano[77,74], L. Cayón[32], A. Chamballu[56], L.-Y Chiang[64], G. Chon[81], P. R. Christensen[84,40], D. L. Clements[56], S. Colafrancesco[48], S. Colombi[61,95], L. P. L. Colombo[25,69], B. Comis[77], A. Coulais[74], B. P. Crill[69,85], F. Cuttaia[51], A. Da Silva[13], H. Dahle[66,12], L. Danese[87], R. J. Davis[70], P. de Bernardis[35], G. de Gasperis[38], G. de Zotti[47,87], J. Delabrouille[1], J. Démoclès[75], J. M. Diego[68], K. Dolag[98,80], H. Dole[60,59], S. Donzelli[52], O. Doré[69,11], U. Dörl[80], M. Douspis[60], X. Dupac[43], G. Efstathiou[65], T. A. Enßlin[80], H. K. Eriksen[66], F. Finelli[51], I. Flores-Cacho[10,97], O. Forni[97,10], M. Frailis[49], E. Franceschi[51], M. Frommert[19], S. Galeotta[49], K. Ganga[1], R. T. Génova-Santos[67], M. Giard[97,10], M. Gilfanov[80,90], Y. Giraud-Héraud[1], J. González-Nuevo[68,87], K. M. Górski[69,100], A. Gregorio[37,49], A. Gruppuso[51], F. K. Hansen[66], D. Harrison[65,72], P. Heinämäki[94], A. Hempel[67,41], S. Henrot-Versillé[73], C. Hernández-Monteagudo[14,80], D. Herranz[68], S. R. Hildebrandt[11], E. Hivon[61,95], M. Hobson[7], W. A. Holmes[69], G. Hurier[77], T. R. Jaffe[97,10], A. H. Jaffe[56], T. Jagemann[43], W. C. Jones[27], M. Juvela[26], E. Keihänen[26], I. Khamitov[93], T. S. Kisner[79], R. Kneissl[42,8], J. Knoche[80], L. Knox[29], M. Kunz[19,60,4], H. Kurki-Suonio[26,46], G. Lagache[60], A. Lähteenmäki[2,46], J.-M. Lamarre[74], A. Lasenby[7,72], C. R. Lawrence[69], M. Le Jeune[1], R. Leonardi[43], P. B. Lilje[66,12], M. López-Caniego[68], G. Luzzi[73], J. F. Macías-Pérez[77], D. Maino[36,52], N. Mandolesi[51,6,34], M. Maris[49], F. Marleau[63], D. J. Marshall[75], E. Martínez-González[68], S. Masi[35], M. Massardi[50], S. Matarrese[33], P. Mazzotta[38], S. Mei[45,96,11], A. Melchiorri[35,53], J.-B. Melin[17], L. Mendes[43], A. Mennella[36,52], S. Mitra[55,69], M.-A. Miville-Deschênes[60,9], A. Moneti[61], L. Montier[97,10], G. Morgante[51], D. Mortlock[56], D. Munshi[88], J. A. Murphy[83], P. Naselsky[84,40], F. Nati[35], P. Natoli[34,5,51], H. U. Nørgaard-Nielsen[18], F. Noviello[70], D. Novikov[56], I. Novikov[84], S. Osborne[92], F. Pajot[60], D. Paoletti[51], F. Pasian[49], G. Patanchon[1], O. Perdereau[73], L. Perotto[77], F. Perrotta[87], F. Piacentini[35], M. Piat[1], E. Pierpaoli[25], R. Piffaretti[75,17], S. Plaszczynski[73], E. Pointecouteau[97,10], G. Polenta[5,48], N. Ponthieu[60,54], L. Popa[62], T. Poutanen[46,26,2], G. W. Pratt[75], S. Prunet[61,95], J.-L. Puget[60], J. P. Rachen[23,80], R. Rebolo[67,16,41], M. Reinecke[80], M. Remazeilles[60,1], C. Renault[77], S. Ricciardi[51], T. Riller[80], I. Ristorcelli[97,10], G. Rocha[69,11], M. Roman[1], C. Rosset[1], M. Rossetti[36,52,⋆], J. A. Rubiño-Martín[67,41], B. Rusholme[57], M. Sandri[51], G. Savini[86], D. Scott[24], G. F. Smoot[28,79,1], J.-L. Starck[75], R. Sudiwala[88], R. Sunyaev[80,90], D. Sutton[65,72], A.-S. Suur-Uski[26,46], J.-F. Sygnet[61], J. A. Tauber[44], L. Terenzi[51], L. Toffolatti[21,68], M. Tomasi[52], M. Tristram[73], J. Tuovinen[82], L. Valenziano[51], B. Van Tent[78], P. Vielva[68], F. Villa[51], N. Vittorio[38], L. A. Wade[69], B. D. Wandelt[61,95,31], N. Welikala[60], D. Yvon[17], A. Zacchei[49], S. Zaroubi[71], and A. Zonca[30]

(Affiliations can be found after the references)

Received 17 July 2012 / Accepted 22 October 2012

ABSTRACT

The survey of galaxy clusters performed by *Planck* through the Sunyaev-Zeldovich effect has already discovered many interesting objects, thanks to its full sky coverage. One of the SZ candidates detected in the early months of the mission near to the signal-to-noise threshold, PLCKG214.6+37.0, was later revealed by *XMM-Newton* to be a triple system of galaxy clusters. We present the results from a deep *XMM-Newton* re-observation of PLCKG214.6+37.0, part of a multi-wavelength programme to investigate *Planck* discovered superclusters. The characterisation of the physical properties of the three components has allowed us to build a template model to extract the total SZ signal of this system with *Planck* data. We have partly reconciled the discrepancy between the expected SZ signal derived from X-rays and the observed one, which are now consistent within 1.2σ. We measured the redshift of the three components with the iron lines in the X-ray spectrum, and confirm that the three clumps are likely part of the same supercluster structure. The analysis of the dynamical state of the three components, as well as the absence of detectable excess X-ray emission, suggests that we are witnessing the formation of a massive cluster at an early phase of interaction.

Key words. galaxies: clusters: general – large-scale structure of Universe – galaxies: clusters: individual: PLCKG214.6+37.0

⋆ Corresponding author: M. Rossetti, e-mail: mariachiara.rossetti@unimi.it

1. Introduction

Clusters of galaxies occupy a special position in the hierarchy of cosmic structures, because they are the largest objects that decoupled from the cosmic expansion and that have had time to undergo gravitational collapse. They are thought to form via a hierarchical sequence of mergers and accretion of smaller systems driven by gravity. During this process the intergalactic gas is heated to high X-ray emitting temperatures by adiabatic compression and shocks and settles in hydrostatic equilibrium within the cluster potential well. Sometimes galaxy clusters are found in multiple systems, super-cluster structures that already decoupled from the Hubble flow and are destined to collapse. The crowded environment of superclusters is an ideal place to study the merging processes of individual components at an early stage of merging and to witness the initial formation phase of very massive structures. Moreover, the processes related to the contraction may increase the density of the intercluster medium and make it observable with current instruments. An example is the central complex of the Shapley concentration, which has been the object of extensive multi-wavelength observations with the aim of characterising the merger processes in galaxy clusters (e.g. Kull & Böhringer 1999; Bardelli et al. 1998; Rossetti et al. 2007; Giacintucci et al. 2005).

Recently a new observational window has opened up for the study of the astrophysics of galaxy clusters through the Sunyaev-Zeldovich effect (Sunyaev & Zeldovich 1972, SZ hereafter): a spectral distortion of the cosmic microwave background (CMB) generated through inverse Compton scattering of CMB photons by thermal electrons in the intracluster medium (ICM). SZ surveys are discovering new clusters, some of which are interesting merging systems (with "El Gordo", Menanteau et al. 2012, being probably the most spectacular example).

A key role in SZ science is now played by the *Planck*[1] satellite. Compared to other SZ surveys of galaxy clusters, *Planck* has only moderate band-dependent spatial resolution, but it possesses a unique nine-band coverage, and more crucially it covers the whole sky. Therefore, it allows the rarest objects to be detected: massive high-redshift systems (Planck Collaboration 2011f), which are the most sensitive to cosmology; and complex multiple systems, which are interesting for the physics of structure formation. Indeed, during the follow-up *XMM-Newton* campaign of *Planck* SZ candidates, we found two new double systems and two new triple systems of clusters (Planck Collaboration 2011c, hereafter Paper I). In all cases, the cumulative contribution predicted by X-ray measurements was lower than the measured SZ signal, although compatible within 3σ.

PLCKG214.6+37.0 is the most massive and the X-ray brightest of the two *Planck* discovered triple systems. The *XMM-Newton* follow-up observations showed that the *Planck* SZ source candidate position is located ~5′ from the two southern components (*A* and *B*). A third subcomponent, *C*, lies approximately 7′ to the north (Fig. 1). The X-ray spectral analysis of component *A* indicated a redshift of $z_{\rm Fe} \sim 0.45$, consistent with two galaxies with spectroscopic redshift of ~0.45, close to the peaks of components *A* and *C*. A cross-correlation with SDSS-DR7 luminous red galaxies and the supercluster catalogue from the SDSS-DR7 (Liivamägi et al. 2012) hinted that this triple system is encompassed within a very large-scale structure located at $z \sim 0.45$, and whose centroid lies about 2 deg to the south (see Appendix B in Paper I for further details).

In this paper we present new SZ measurements of this object with *Planck* and compare them with the results from a a deep *XMM-Newton* re-observation. In Sect. 2 we describe the analysis methods and the *Planck* and *XMM-Newton* data used in this paper. In Sect. 3 we present our results obtained with X-ray and, in Sect. 4, compare them with available optical data from SDSS. In Sect. 5 we compare the X-ray results with *Planck* results. In Sect. 6 we discuss our findings.

Throughout the paper we adopt a ΛCDM cosmology with $H_0 = 70$ km s^{-1} Mpc^{-1}, $\Omega_{\rm M} = 0.3$, and $\Omega_\Lambda = 0.7$. At the nominal redshift of the supercluster, $z = 0.45$, one arcminute corresponds to 350 kpc.

2. Observations

2.1. Planck data and analysis

Planck (Tauber et al. 2010; Planck Collaboration 2011a) is the third-generation space mission to measure the anisotropy of the CMB. It observes the sky in nine frequency bands covering 30–857 GHz with high sensitivity and angular resolution from 31′ to 5′. The Low Frequency Instrument (LFI; Mandolesi et al. 2010; Bersanelli et al. 2010; Mennella et al. 2011) covers the 30, 44, and 70 GHz bands with amplifiers cooled to 20 K. The High Frequency Instrument (HFI; Lamarre et al. 2010; Planck HFI Core Team 2011a) covers the 100, 143, 217, 353, 545, and 857 GHz bands with bolometers cooled to 0.1 K. Polarisation is measured in all but the two highest bands (Leahy et al. 2010; Rosset et al. 2010). A combination of radiative cooling and three mechanical coolers produces the temperatures needed for the detectors and optics (Planck Collaboration 2011b). Two data processing centres (DPCs) check and calibrate the data and make maps of the sky (Planck HFI Core Team 2011b; Zacchei et al. 2011). *Planck*'s sensitivity, angular resolution, and frequency coverage make it a powerful instrument for Galactic and extragalactic astrophysics, as well as for cosmology. Early astrophysics results are given in Planck Collaboration (2011h–z).

Our results are based on the SZ signal as extracted from the six bands of HFI corresponding to the nominal *Planck* survey of 14 months, during which the whole sky was observed twice. We refer to Planck HFI Core Team (2011b) and Zacchei et al. (2011) for the generic scheme of TOI processing and map making, as well as for the technical characteristics of the maps used. We adopted a circular Gaussian as the beam pattern for each frequency, as described in Planck HFI Core Team (2011b); Zacchei et al. (2011).

The total SZ signal is characterised by the integrated Compton parameter Y_{500} defined as $D_{\rm A}^2(z)Y_{500} = (\sigma_{\rm T}/m_{\rm e}c^2)\int P_{\rm th}{\rm d}V$, where $D_{\rm A}(z)$ is the angular distance to a system at redshift z, $\sigma_{\rm T}$ is the Thomson cross-section, c the speed of light, $m_{\rm e}$ the rest mass of the electron, $P_{\rm th}$ the pressure of thermal electrons, and the integral is performed over a sphere of radius R_{500}.

The extraction of the total SZ signal for this structure is more complicated than for single clusters. Owing to its moderate spatial resolution, *Planck* is not able to separate the contributions of the three components from the whole signal. In Paper I, we estimated the total flux assuming a single component with mass corresponding to the sum of the masses of the three clumps,

[1] *Planck* (http://www.esa.int/Planck) is a project of the European Space Agency (ESA) with instruments provided by two scientific consortia funded by ESA member states (in particular the lead countries: France and Italy) with contributions from NASA (USA), and telescope reflectors provided in a collaboration between ESA and a scientific consortium led and funded by Denmark.

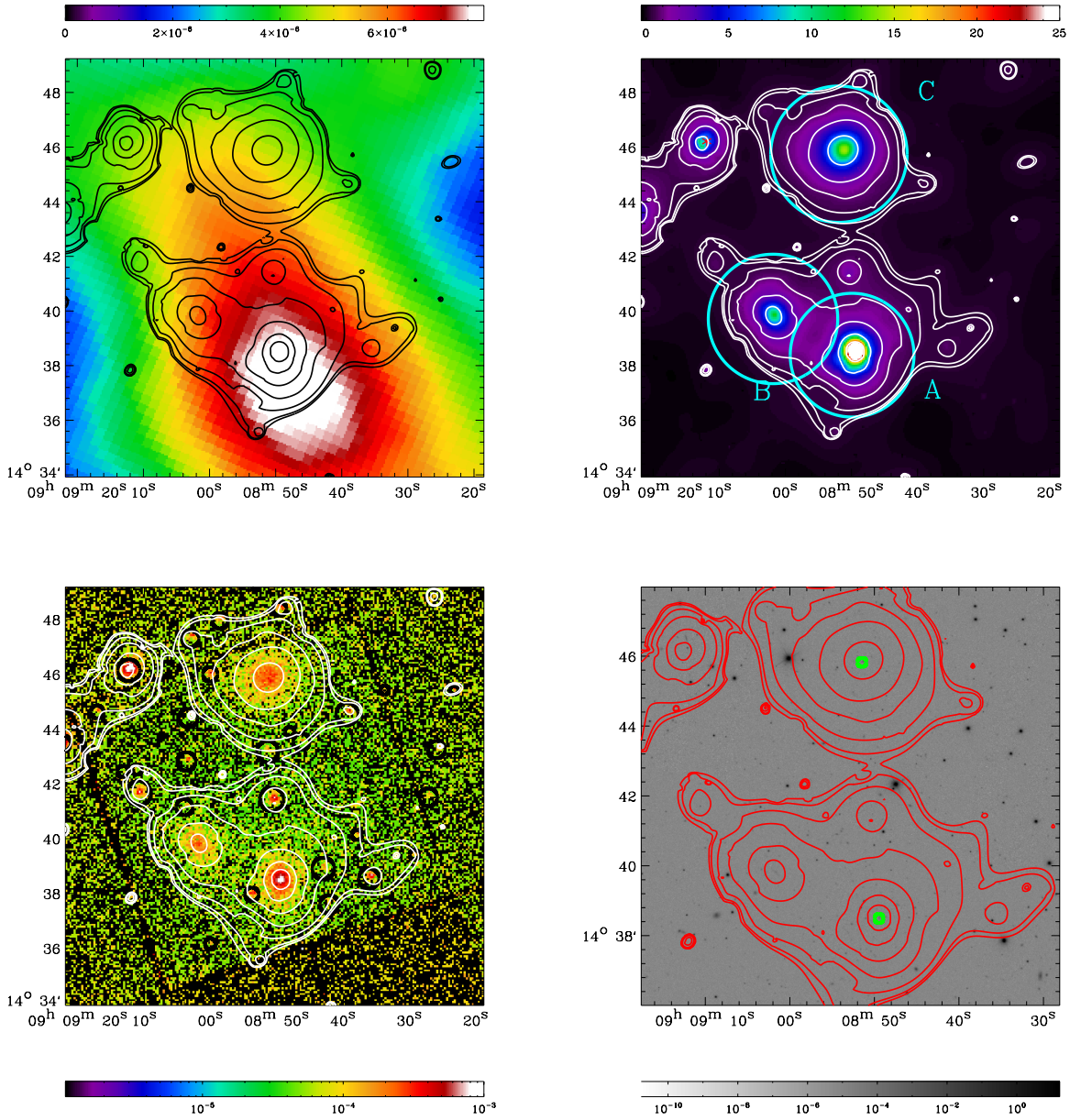

Fig. 1. Triple systems PLCKG214.6+37.0. *Left upper panel*: *Planck* SZ reconstructed map (derived from the Modified Internal Linear Combination Analysis, Hurier et al. 2010), oversampled and smoothed for display purposes. *Right upper panel: XMM-Newton* wavelet filtered image in the [0.5–2.5] keV range (Sect. 2.2). The three components of PLCKG214.6+37.0 are marked with circles (with radius R_{500}, see Table 1) and indicated with letters as in the text. The X-ray structure visible in the north-east (marked with an asterisk) is likely associated with the active galaxy SDSSJ090912.15 + 144613.7, with a spectroscopic redshift $z = 0.767$. *Left lower panel:* Raw MOS count rate (counts s^{-1}) image in the [0.5–2.5] keV range, corrected for vignetting. The black circles mark the point sources detected by our algorithm, which we masked during the analysis (Sect. 2.2). The pixel size in this image is 4.35″. *Right lower panel:* SDSS *r*-band image of the PLCKG214.6+37.0 field. In all panels, north is up and east to the left, and we overlay X-ray contours, computed on the wavelet-filtered image logarithmically spaced starting from the level where a connection is seen between all components (Sect. 3.4).

following a universal pressure profile (Arnaud et al. 2010) centred at the barycentre of the three components. This is obviously only a simple first-order approach. The wealth of information that is now available on this system has allowed us to build a more representative model. With the X-ray constraints on the structural properties of clumps *A*, *B*, and *C* (Sect. 3.1), we are now able to build a three-component model. As discussed in Planck Collaboration (2011d), our baseline pressure profile is the standard "universal" pressure profile derived by Arnaud et al. (2010). We assumed this profile for each clump, parametrised in size by the respective X-ray scale radius, R_{500}. The normalisations, expressed as integrated Comptonisation parameters within $5\,R_{500}$ were tied together according to the ratio of their respective $Y_{X,500}$ values, as determined from the X-ray analysis. Thus only one overall normalisation parameter remains to be determined. Such a template used under these assumptions and parametrisations, together with the multi-frequency matched filter algorithm, MMF3 (Melin et al. 2006), directly provides the integrated SZ flux over the whole structure.

The two-dimensional reconstruction of the Comptonisation parameter, $y = (\sigma_T/m_e c^2) \int P_{th} dl$, provides a way to map the spatial distribution of the thermal pressure integrated along the line of sight. This is performed using the modified internal linear combination method (MILCA, Hurier et al. 2010) on the six *Planck* all-sky maps from 100 GHz to 857 GHz. MILCA is a component separation approach aimed at extracting a chosen component (here the thermal SZ signal) from a multi-channel set of input maps. It is primarly based on the ILC approach (e.g., Eriksen et al. 2004), which searches for the linear combination of the input maps that minimises the variance of the final reconstructed map imposing spectral constraints.

2.2. XMM-Newton observation and data reduction

PLCKG214.6+37.0 was observed again by *XMM-Newton* during AO10, for a nominal exposure time of 65 ks. We produced calibrated event files from observation data files (ODF) using v.11.0 of the *XMM-Newton* Science Analysis Software (SAS). We cleaned the event files from soft proton flares, using a double filtering process (see Bourdin & Mazzotta 2008 for details). After the cleaning, the net exposure time is ~47 ks for the MOS detectors and ~37 ks for the pncamera. Since a quiescent component of soft protons may survive the procedure described above, we calculated the "in over out ratio" R_{SB} (De Luca & Molendi 2004) and found values close to unity, suggesting a negligible contribution of this component. We masked bright point sources, detected in the MOS images as described in Bourdin & Mazzotta (2008). We performed the same data reduction procedure on the snapshot observation 0656200101, finding a cleaned exposure time of ~15 ks for the MOS and ~10 for the pn.

We then combined the two observations and binned the photon events in sky coordinates and energy cubes, matching the angular and spectral resolution of each focal instrument. For spectroscopic and imaging purposes, we associated an "effective exposure" and a "background noise" cube to this photon cube (see Bourdin et al. 2011 for details). The "effective exposure" is computed as a linear combination of CCD exposure times related to individual observations, with local corrections for useful CCD areas, RGS transmissions, and mirror vignetting factors. The "background noise" includes a set of particle background spectra modelled from observations performed with the closed filter. Following an approach proposed in e.g., Leccardi & Molendi (2008) or Kuntz & Snowden (2008), this model sums a quiescent continuum to a set of fluorescence emission lines convolved with the energy response of each detector. Secondary background noise components include the cosmic X-ray background and Galactic foregrounds. The cosmic X-ray background is modelled with an absorbed power law of index $\Gamma = 1.42$ (e.g., Lumb et al. 2002), while the Galactic foregrounds are modelled by the sum of two absorbed thermal components accounting for theGgalactic transabsorption emission ($kT_1 = 0.099$ keV and $kT_2 = 0.248$ keV, Kuntz & Snowden 2000). We estimate emissivities of each of these components from a joint fit of all background noise components in a region of the field of view located beyond the supercluster boundary.

To estimate average ICM temperatures, kT along the line of sight and for a given region of the field of view, we added a source emission spectrum to the "background noise", and fitted the spectral shape of the resulting function to the photon energy distribution registered in the 0.3–10 keV energy band. In this modelling, the source emission spectrum assumes a redshifted and nH absorbed emission modelled from the Astrophysical Plasma Emission Code (APEC, Smith et al. 2001), with the element abundances of Grevesse & Sauval (1998) and neutral hydrogen absorption cross-sections of Balucinska-Church & McCammon (1992). It is corrected for effective exposure, altered by the mirror effective areas, filter transmissions and detector quantum efficiency, and convolved by a local energy response matrix.

The X-ray image shown in Fig. 1 (upper left) is a wavelet-filtered image, computed in the 0.5–2.5 keV energy band. To generate this image, we corrected the photon map for effective exposure and soft-thresholded its undecimated B3-spline wavelet coefficients (Starck et al. 2007) to a 3σ level. In this procedure, significance thresholds have been directly computed from the raw (Poisson distributed) photon map, following the multi-scale variance stabilisation scheme introduced in Zhang et al. (2008). We applied the same transformation to a "background noise" map, which we then subtracted from the image. The wavelet filtering allows us to reduce the amplitude of the noise that dominates the raw images (see Fig. 1, lower left) and to map the distribution of the ICM on different scales (see the pioneering works by Slezak et al. 1994; Vikhlinin et al. 1997; Starck & Pierre 1998).

3. Structure of the clusters from X-rays

3.1. Global analysis of the cluster components

Assuming that the three structures are located at the same redshift, $z = 0.45$ (the spectroscopic value found in Paper I), from the combination of the two *XMM-Newton* observations we have carried out an X-ray analysis for each component independently (we masked the two other clumps while analysing the third one). We extracted surface brightness profiles of each component, centred on the X-ray peak, in the energy band 0.5–2.5 keV. We used the surface brightness profile to model the three-dimensional density profile: the parametric density distribution (Vikhlinin et al. 2006) was projected, convolved with the PSF and fitted to the observed surface brightness profile (Bourdin et al. 2011). From the density profile we measured the gas mass, M_g, which we combined with the global temperature T_X, obtained with the spectral analysis, to measure $Y_X = M_g * T_X$ (Kravtsov et al. 2006). We used the M_{500}–Y_X scaling relation in Arnaud et al. (2010) to estimate the total mass M_{500}, defined as the mass corresponding to a density contrast $\delta = 500$ with respect to the critical density at the redshift of the cluster, $\rho_c(z)$, thus $M_{500} = (4\pi/3)500\rho_c(z)R^3_{500}$. The global cluster parameters were estimated iteratively within R_{500}, until convergence.

The resulting global X-ray properties are summarised in Table 1. The Y_X and M_{500} values are slightly higher, but consistent within 1.5σ, with the results presented in Paper I.

3.2. Redshift estimates

Crucial information on the nature of this triple system comes from measuring the redshift of each component, allowing us to assess whether this is a bound supercluster structure or a combination of unrelated objects along the same line of sight. In Paper I, a reliable redshift measurement, obtained with the short *XMM-Newton* observation, was only available for component *A*. Its value ($z = 0.45$) was consistent with the only two spectroscopic redshifts available in this field and corresponding to the bright central galaxies in components *A* (SDSSJ090849.38 + 143830.1 $z = 0.450$) and *C* (SDSSJ090851.2 + 144551.0 $z = 0.452$). A photometric redshift, $z = 0.46$, was furthermore

Table 1. Physical properties of the components of PLCKG214.6+37.0.

Component	RA_X [hh:mm:ss]	Dec_X [hh:mm:ss]	T_X [keV]	$M_{g,500}$ [$10^{14}\ M_\odot$]	Y_X [$10^{14}\ M_\odot$ keV]	M_{500} [$10^{14}\ M_\odot$]	R_{500} [kpc]
A	09:08:49.6	+14:38:26.8	3.6 ± 0.4	0.26 ± 0.01	0.96 ± 0.11	2.22 ± 0.16	784 ± 19
B	09:09:01.8	+14:39:45.6	4.3 ± 0.9	0.28 ± 0.02	1.2 ± 0.3	2.5 ± 0.4	820 ± 40
C	09:08:51.2	+14:45:46.7	5.3 ± 0.9	0.30 ± 0.02	1.6 ± 0.3	3.0 ± 0.3	864 ± 33

Table 2. Redshift measurements from the X-ray iron line for the components of PLCKG214.6+37.0.

Component	MOS1	MOS2	pn	Joint fit
A	0.447 (−0.013 + 0.024)	0.446 (−0.005 + 0.013)	0.441 (−0.009 + 0.009)	0.445 (−0.006 + 0.006) (m1+m2+pn)
B	0.529 (−0.018 + 0.024)	0.472 (−0.008 + 0.063)	0.475 (−0.016 + 0.023)	0.481 (−0.011 + 0.013) (m2+pn)
C	0.469 (−0.020 + 0.020)	0.434 (−0.016 + 0.017)	0.463 (−0.017 + 0.009)	0.459 (−0.010 + 0.010) (m1+m2+pn)

available for a bright galaxy (SDSSJ090902.66 + 143948.1) very close to the peak of component *B*.

With the new *XMM-Newton* observation, we detect the iron K complex in each clump. We extracted spectra in a circle centred on each component with radius R_{500} (Table 1). We performed a more standard spectral extraction and analysis than the one described in Sect. 2.2, extracting in each region the spectrum for each detector and its appropriate response (RMF) and ancillary (ARF) files. We fitted spectra within XSPEC, modelling the instrumental and cosmic background as in Leccardi & Molendi (2008), leaving as free parameters of the fit the temperature, metal abundance, redshift, and normalisation of the cluster component (see Planck Collaboration 2011c for details). We first fitted spectra for each detector separately. While the MOS detectors do not show any instrumental line in the whole 4–5 keV range (Leccardi & Molendi 2008), the pn detector shows a faint fluorescent line[2] in the spectral range where we expect to find the redshifted cluster line. We verified that this feature does not significantly affect our results, since the pn redshift and metal abundance are always consistent with at least one of the MOS detectors. We report our results in Table 2.

For components *A* and *C* the redshift measurements for each detector are consistent within 1σ and we performed joint fits combining all instruments (Table 2). For component *B*, the redshift measurement with MOS1 is higher than the estimates with the other detectors, although consistent within 2σ. The joint fit of the three detectors in this case would lead to a best fit value $z = 0.516\,(-0.023, +0.014)$, while combining only MOS2 and pn we find $0.481\,(-0.011, +0.013)$. In the joint fit of the three detectors, the MOS1 spectrum drives the redshift estimate, leaving many residuals around the position of the iron lines for the MOS2 and pn spectra. We performed simulations within XSPEC to quantify the probability that, given the statistical quality of the spectra and the source-to-background ratio, a redshift measurement as high as $z = 0.529$, may result just from statistical fluctuations of a spectrum with $z = 0.48$. We assumed the best fit model of the joint MOS2 and pn analysis as the input source and background model with a redshift $z = 0.48$ and we generated 1500 mock spectra that we fitted separately with the same procedure we used for the real spectrum. We found a higher redshift than what we measured with MOS1 in 3% of the simulated spectra. With these simulations, we also reproduced the joint fit procedure: we performed 500 joint fits of three simulated spectra and found that a redshift as high as 0.516 occurs with less than 1% probability. Furthermore, we performed other simulations assuming the redshift resulting from the joint fit of the three detectors, $z = 0.516$: the probability of finding two redshifts as low as $z = 0.475$ is about 1.7%. The simulations we have described show that it is unlikely that the three redshift measurements and the joint fit we obtained for subcluster *B* may result from statistical fluctuations of the same input spectrum, suggesting a systematic origin for the discrepancy between MOS1 and the other detectors. Indeed, the quality of the fit with the MOS1 data alone is worse than with the other detectors, exhibiting strong residuals around the best fit model. We verified the possibility of a calibration issue affecting MOS1 by checking the position of the instrumental lines: we did not find any significant systematic offset for the bright low-energy Al and Si lines, but the absence of strong fluorescent lines between 2 and 5.4 keV did not allow us to test the calibration in the energy range we are interested in. Although the origin of the systematic difference of the MOS1 spectrum is still unclear, we decided to exclude this detector when estimating the redshift of component *B* (Table 2). Nonetheless, in the following, we also discuss the possibility that the cluster is located at the higher redshift $z = 0.516$. Concerning the components *A* and *C*, the redshift measurements are not significantly affected if we exclude the MOS1 detector.

The redshift estimates we obtained from X-ray data for components *A* ($z = 0.445 \pm 0.006$) and *C* ($z = 0.46 \pm 0.01$) are nicely consistent with the spectroscopic values found in the SDSS archive for their central brightest galaxies (0.450 and 0.452, respectively). Concerning component *B*, even without considering the MOS1 detector, we still find a higher best fit value ($z = 0.48 \pm 0.01$) with respect to the other two components. This is shown in Fig. 2, where we compare the variation of χ^2 for the joint fits (see Table 2) of the three components. While component *A* and *C* are consistent with being at the same redshift at less than 1σ, component *B* is likely located at a higher redshift, although consistent at less than 2σ with the position of the other clusters. Therefore, component *B* is likely separated along the line of sight from the two other components by 69 (−30, +25) Mpc (150 Mpc, if we consider the redshift estimate obtained with the three detectors). While this large separation suggests that the cluster *B* is not interacting with the other components, it is still consistent with the three objects being part of the same supercluster structure (Bahcall 1999).

Using the best fit redshift estimates for the three components, we recomputed the physical parameters in Table 1. While the variations for cluster *A* and *C* are negligible, for cluster *B* we found $Y_X = (0.74 \pm 0.19) \times 10^{14}\ M_\odot$ keV, $M_{500} = (1.89 \pm 0.20) \times 10^{14}\ M_\odot$ and $R_{500} = (726 \pm 25)$ kpc.

[2] Ti K_α, http://xmm2.esac.esa.int/external/xmm_sw_cal/background/filter_closed/pn/mfreyberg-WA2-7.ps.gz

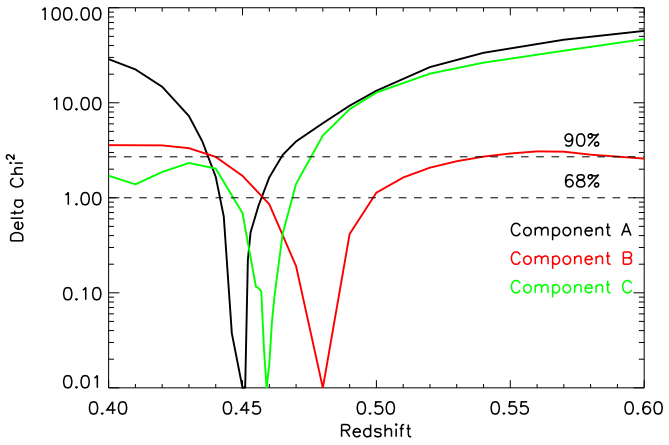

Fig. 2. Variation in χ^2 when fitting the spectra for the redshift measurement. Black, red, and green lines represent component *A*, *B*, and *C*, respectively. Thin dashed lines correspond to the 68% and 90% error ranges, respectively.

3.3. Radial structural analysis of the components

We performed a radial analysis of the X-ray observations of PLCKG214.6+37.0 to study the behaviour of the main thermodynamical quantities of the ICM. We extracted the surface brightness profile as discussed in Sect. 3.1: while the *A* component shows a very peaked profile, which might indicate a cool core state, the *B* and *C* components have flatter profiles at the centre, a signature of an un-relaxed dynamical state. On a more quantitative basis, we extracted the three-dimensional density profiles for each component, with the parametric procedure discussed in Sect. 3.1, and computed the scaled central density, $n_0 E(z)^{-2}$, where $E(z)^2 = \Omega_M(1+z)^3 + \Omega_\Lambda$ is the ratio of the Hubble constant at redshift z with respect to its present value H_0. This parameter can be used to classify clusters into cool-core ($n_0 E(z)^{-2} > 4 \times 10^{-2}\,\mathrm{cm}^{-3}$) and non cool-core objects (Pratt et al. 2009). As expected, *A* shows a central density ($n_0 E(z)^{-2} = 7 \times 10^{-2}\,\mathrm{cm}^{-3}$) typical of cool-core objects, while *B* and *C* show much lower central densities ($n_0 E(z)^{-2} = 2 \times 10^{-3}\,\mathrm{cm}^{-3}$, both).

We extracted spectra in four (three for component *C*) annuli and fitted them with a single-temperature absorbed model, fixing as many components as we could because of the faintness of the source: *nH* was fixed to the Galactic value (Dickey & Lockman 1990), redshift of the three components to 0.45; and we also fixed all parameters of the background components. In most cases we also fixed the metallicity to $0.3\,Z_\odot$, except in the centre of subcluster *A*, where we could estimate an excess of metal abundance ($Z = 0.6 \pm 0.1\,Z_\odot$), as often found in cool cores. All temperature profiles are consistent at 1σ with being flat and with the global values shown in Table 1, therefore from now on we will consider them to be isothermal.

We combined the three-dimensional density profile and the global temperature to derive two other thermodynamic quantities: pressure and entropy[3]. Pressure is especially relevant to our analysis since it is the quantity that is measured directly through the SZ effect. We have fitted the profiles with the model described in Arnaud et al. (2010), and the best fit parameters are consistent with the ones for relaxed cool core objects for component *A*, and for disturbed objects for components *B* and *C*.

Entropy is a thermodynamic quantity that is connected both to the accretion history of the cluster and to non gravitational processes. If we fit the profile with a power law plus a constant, the central entropy K_0 is a good indicator of the cool core state (Cavagnolo et al. 2009). The central entropy values are essentially driven by the central densities because we assumed a constant temperature, given the large uncertainties and poor resolution of the temperature profiles. As expected, for subcluster *A* we found $K_0 = (13 \pm 2)\,\mathrm{keV\,cm}^2$, a central entropy typical of cool core systems, while for *B* and *C* we found higher values ($K_0 = 142 \pm 10\,\mathrm{keV\,cm}^2$ and $K_0 = 153 \pm 18\,\mathrm{keV\,cm}^2$, respectively) typical of unrelaxed objects.

3.4. 2D structure of the components and of the supercluster

A qualitative analysis of the X-ray image (Fig. 4) shows that the two southern components are apparently connected. Indeed the X-ray surface brightness isophotes of component *B* (Fig. 1) are slightly elongated in the direction of component *A*, as often observed in pairs of merging clusters (e.g., the three systems in Maurogordato et al. 2011; and the pair A399-A401 in Sakelliou & Ponman 2004). We visually investigated the possible connection between the components by drawing constant surface brightness contours in the X-ray image. The appearance of the contours may provide information about the two-dimensional distribution of the intracluster gas and the possible contamination by residual point sources. A connection between the components *A* and *B* is robustly detected, at a contour level above the background intensity (inner contour in Fig. 4). However, with this simple analysis it is not possible to assess whether this connection is physical or only a projection effect. We used the same method between *A* and *C* where we start to see a connection at a much lower intensity, about 25% of the level of the background model in the same region (outer contour in Fig. 4). In this regime, it might still be possible that the connection between the two components is due to uncertainties in background estimation or to residual point sources.

On a more quantitative basis, we extracted longitudinal surface brightness profiles in the east-west direction across components *A* and *B*, and in the north-south direction, across components *A* and *C* (in the boxes shown in Fig. 4). The profile across components *A* and *B* (Fig. 5, left panel) shows clearly enhanced emission with respect to the opposite direction between the two clumps: we modelled the emission of each component by taking the data in the external part of the pair and projecting it symmetrically in the direction of the possible interaction. In the region where the two emissions overlap, we summed the two models and found their sum to be consistent with the data. The two objects are very close in the plane of the sky and their emissions apparently overlap at less than R_{500} (Fig. 1); if they were located at the same distance from us and interacting we would expect to see compression and enhanced X-ray emission between the two objects. This is not the case here, so our results argue in favour of a separation along the line of sight of the two components, possibly still in an early phase of interaction.

Concerning components *A* and *C*, their separation in the plane of the sky is 7.4′, corresponding to ∼2.5 Mpc at $z = 0.45$. The analysis of the longitudinal surface brightness profile across them (Fig. 5, right panel) confirms our earlier indication: the emission in the intersection region is not significantly detected and is consistent with the "undisturbed" model (derived as before).

[3] The "X-ray astronomer's entropy" is defined as $K = kT/n_e^{2/3}$, where n_e is the electron density and T the X-ray temperature. This quantity is related to the thermodynamic entropy by a logarithm and an additive constant.

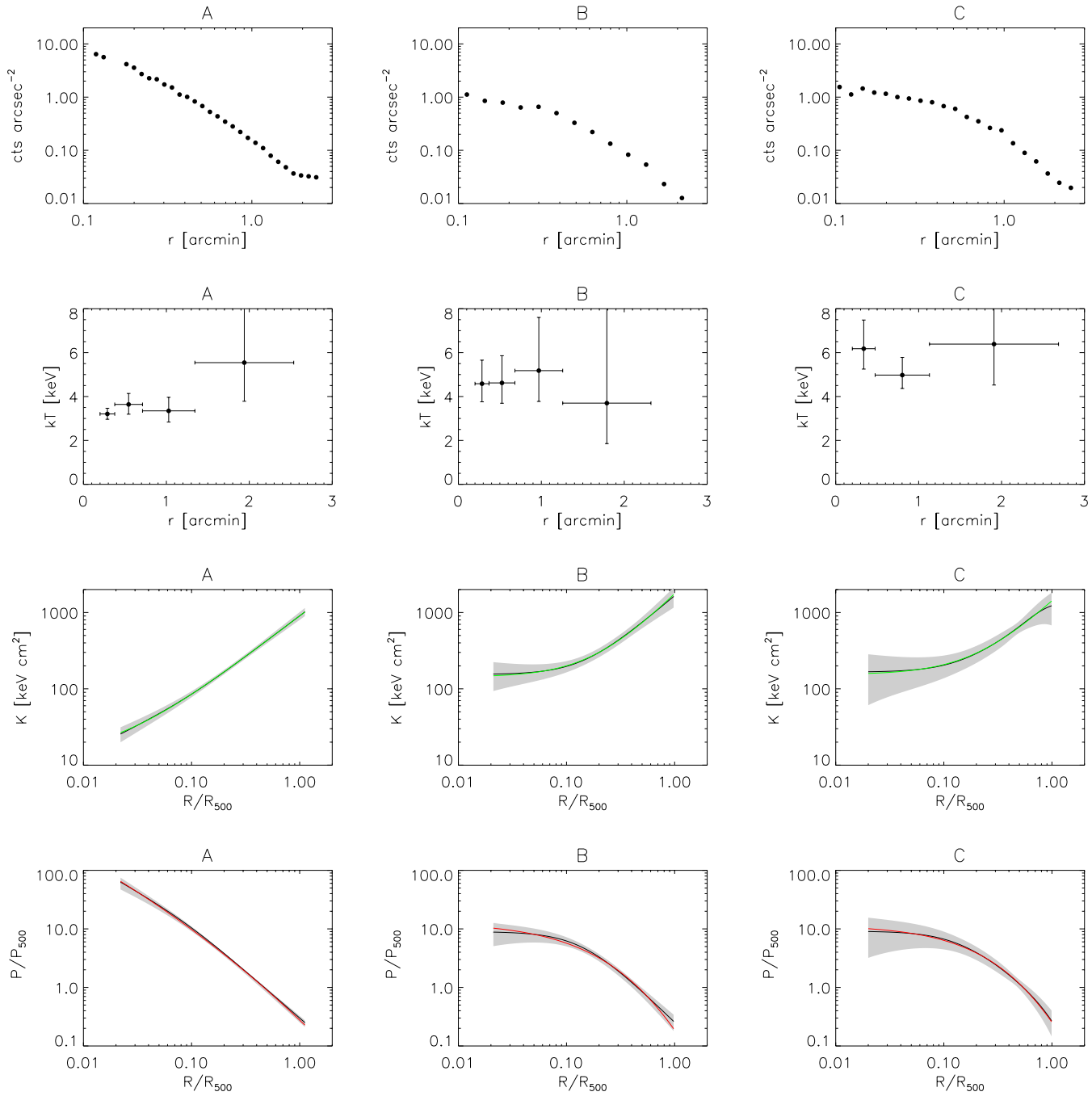

Fig. 3. Radial profiles for the relevant X-ray quantities for each component. *From top to bottom*: surface brightness in the energy band 0.5–2.5 keV, projected temperature, three-dimensional entropy and pressure both as a function of the projected distance from the ce (rescaled by the value at R_{500}) The first two quantities are functions of the projected distance from the centre and the others are functions of the distance from the centre in units of R_{500} (with the values in Table 1). The black lines in the last two rows are the combination of the density and temperature profiles to estimate entropy and pressure and the shaded areas show the corresponding $\pm 1\sigma$ uncertainty. The red and green lines are our best fit models, with the functions discussed in the text.

These results suggest that the three clusters, while likely belonging to the same structure, have not started to fully interact yet.

4. Comparison with optical data

Since the sky region of PLCKG214.6+37.0 is covered by the Sloan Digital Sky Survey (SDSS)[4], we retrieved a galaxy catalogue from SDSS Data Release 8 (DR8). It covers a circular area of 20′ radius around the barycentre of PLCKG214.6+37.0 and includes optical magnitudes and photometric redshifts (see Abazajian et al. 2009, for a description of measurements and calibration of photometric readshifts in SDSS DR8). It contains about 2000 objects, around 900 of which are in the redshift range 0.35–0.6. Unfortunately, spectroscopic redshifts are available only for the brightest central galaxies of components *A* and *C*, thus we relied on photometric redshifts alone in our analysis. Spectroscopic information on this system will be available

[4] http://www.sdss.org/

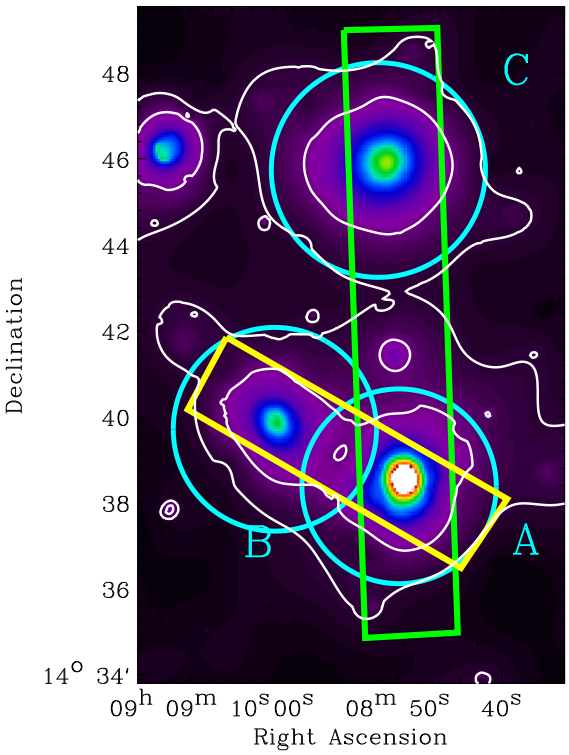

Fig. 4. *XMM-Newton* wavelet filtered image of PLCKG214.6+37.0. Contours overlaid correspond to the levels where we start to see connection between the components. The green and yellow regions show where we extracted longitudinal profiles.

from our follow-up programme and will be discussed in a forthcoming paper.

4.1. Photometric redshifts of the three components

We used the archival photometric redshifts in our catalogue to estimate the redshift of the three components. We extracted a sub-catalogue selecting only galaxies in the photometric redshift range 0.35–0.6 and, for each clump, we calculated the median redshift of the galaxy population around the X-ray centre as a function of the cutoff radius. The resulting plot is shown in Fig. 6. Components *A* and *C* are both consistent with the spectroscopic value of their central galaxies ($z = 0.45$), but the innermost 2′ of component *B* indicate a slightly higher redshift ($z_{\rm phot} \simeq 0.47$), similar to the results of the X-ray analysis, although consistent at 2σ with the values of the other components. At larger radii, the redshift estimates for the three clumps are all consistent with each other. It should be noted however that components *A* and *B* are separated only by ≃2 arcmin, thus all the estimates at similar or larger radii may be contaminated by galaxies belonging to the other cluster.

4.2. Optical appearance and morphology of the cluster

We used the catalogue from SDSS to build two-dimensional galaxy density maps in different photometric redshift cuts (Fig. 7), with a width $\Delta z_{\rm phot} = 0.04$. We assigned the galaxies to a fine grid of 24″ per pixel, which is then degraded with a Gaussian beam to an effective resolution of 3′. We also computed a significance map using as reference ten random non-overlapping control regions in a 9 deg^2 area around the system.

Clear galaxy overdensities show up around $z_{\rm phot} = 0.46$ at the location of the three X-ray clumps. However, these overdensities do not appear isolated. At the location of cluster *B*, we see an overpopulation of galaxies towards higher redshift (5σ peak at $z_{\rm phot} \sim 0.5$), consistent with the redshift $z = 0.48$ we found in X-rays, whereas the overdensity extends towards slightly lower redshifts ($z_{\rm phot} \sim 0.42$) at the position of cluster *A*. There are also indications of another concentration close to component *B* at higher redshift (0.52–0.6).

We investigated the maps in Fig. 7 to look for a possible population of inter-cluster galaxies: i.e., objects not associated with one of the three clumps but rather with the whole structure, which would support a scenario where the three clumps are physically connected. We draw iso-contours levels in the significance map (Fig. 7): the outermost contour between 0.44 and 0.52 connecting the three clumps indicates the presence of a 3σ excess in the galaxy number density above background in the inter-cluster region.

5. Comparison with *Planck*

5.1. Total SZ signal

As a simple comparison of the SZ and X-ray properties, we can compare the *Planck Y* measurement with the predicted values from the sum of the $Y_{\rm X}$ estimates of all three components, using the scaling relations in Arnaud et al. (2010). From our X-ray estimates (Table 1), we predict the total integrated value of the Comptonisation parameter within a sphere of radius $5\,R_{500}$ for the sum of the three components to be $Y_{x,5\,R500} = (7.52 \pm 0.9) \times 10^{-4}$ arcmin^2. This is about 50% of the measured signal in the same region which was found in Paper I and the two values are compatible within $2.3\,\sigma$.

In the following, we work under the assumption that the three clusters are all located at the same redshift $z = 0.45$. Considering the best fit redshift for component *B* leads to a slightly smaller SZ flux $Y_{x,5\,R500} = (6.44 \pm 0.7) \times 10^{-4}$ arcmin^2.

As discussed in Sect. 2.1, we used the parameters provided in Table 1 to improve our estimate of the total SZ signal of this structure from *Planck* data. We built a specific template from the X-ray analysis, made from three universal pressure profiles cut to $5\,R_{500}$ (Arnaud et al. 2010) corresponding to the three components. Each component is placed at its precise coordinates and the size is given by the R_{500} value in Table 1. We also fixed the relative intensity between the components to verify $A/C = 0.96/1.61$ and $B/C = 1.22/1.61$ for the ratio of integrated fluxes. Then we ran the MMF3 algorithm (Melin et al. 2006) to estimate the amplitude of the template (and hence the total SZ signal of the whole system), and we found $Y_{5\,R_{500}} = (12 \pm 3) \times 10^{-4}$ arcmin^2, when centring the map on component *B*[5]. Our estimate of the supercluster SZ flux is slightly larger than the X-ray prediction but consistent at $\simeq 1.3\sigma$ (1.8σ using $z = 0.516$ for component *B*). We further allowed the position of the template to be a free parameter and found that the algorithm is able to reconstruct the position of the peak with a positional accuracy of one sky pixel (1.7×1.7 arcmin^2, in a HEALPIX projection of $N_{\rm side} = 2048$,

[5] The MMF3 algorithm estimates the noise (instrumental and astrophysical) in a region of 10×10 deg^2 around the centre (excluding the region within $5R_{500}$), therefore changing the centring from one component to the other can affect the background estimation and hence the flux and signal-to-noise ratio. Centring maps on component *A* we found $Y_{5R_{500}} = (10 \pm 3) \times 10^{-4}$ arcmin^2 and on *C* $Y_{5R_{500}} = (13 \pm 3) \times 10^{-4}$ arcmin^2. Our SZ flux estimations are all compatible with each other.

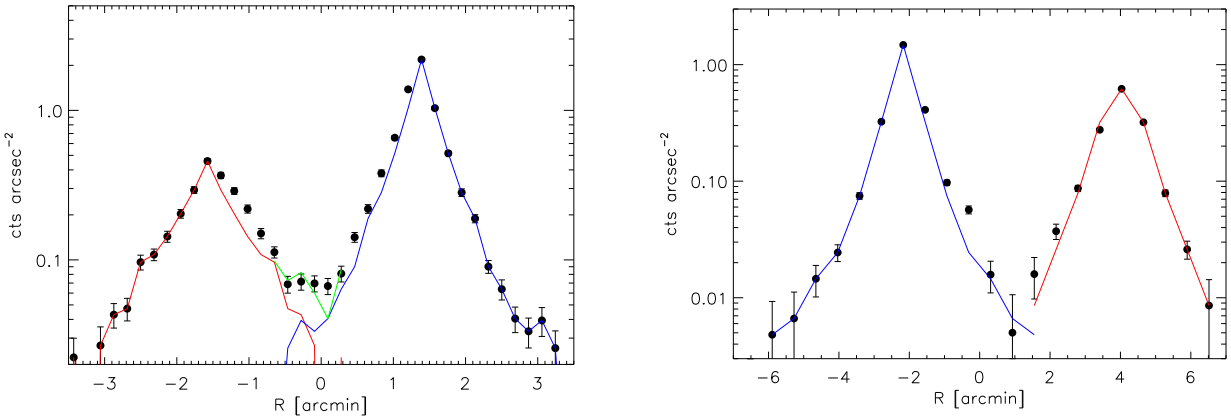

Fig. 5. X-ray Longitudinal profile in the east-west (*left panel*) and north-south directions (*right panel*). *Left panel*: negative distances correspond to component *B*, positive ones to component *A*. The red and blue lines show the "undisturbed" models for components *B* and *A* (see text), respectively, while the green line in the intersection region is the sum of the two models. *Right panel*: negative distances correspond to component *A*, positive ones to component *C*. The red and blue lines show the "undisturbed" models for components *A* and *C*, respectively (see text).

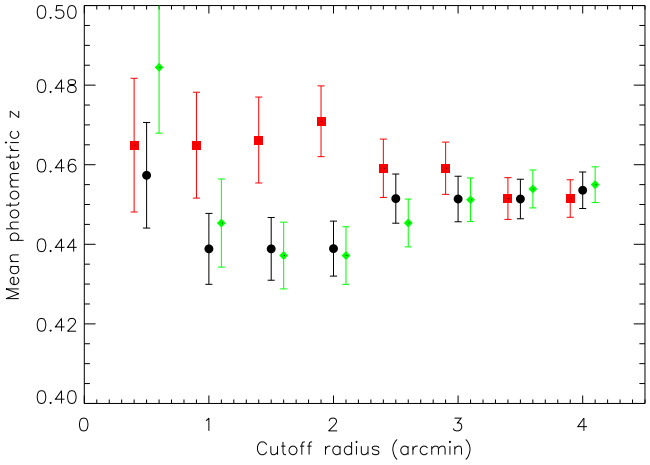

Fig. 6. Median photometric redshifts for the three clumps (*A* black circles; *B* red squares; *C* green diamonds) of all the galaxies within the cut-off radius. The error bars are the standard deviations of the photometric redshifts distributions. Given the small separation between components *A* and *B*, the points at radii $\gtrsim 2'$ may be contaminated by galaxies of the other structure.

Górski et al. 2005). This is consistent with the positional accuracy of the MMF3 algorithm, which has been tested both on simulations and on real data with known clusters.

The discrepancy between the observed SZ signal and the prediction from the Y_X measurement is decreased with respect to Paper I: while the X-ray prediction was only 40% of the SZ measurement, it is now between 60 and 77%, depending on the map centring. This is partly due to the higher Y_X values we found in this analysis with respect to Paper I, especially for components *B* and *C*. It is also certainly due to the improved accuracy of the HFI maps obtained with two full surveys of the sky and to the multi-component model we have used to estimate the SZ flux, with respect to the data from the first sky survey and to the single component model that was used in Paper I. Indeed, these results confirm our capability to extract faint SZ signals, when guided by X-ray priors (Planck Collaboration 2011e).

5.2. SZ signal distribution

It is possible to combine the X-ray images with the temperatures of the components to predict the distribution of the SZ signal (see Mroczkowski et al. 2012, for a similar approach). X-ray images in the soft band are proportional to the square of the density integrated along the line of sight and therefore their square root can be combined with a temperature map to derive a pseudo-pressure map[6], which when smoothed with the *Planck* resolution, can be qualitatively compared with the *y*-maps. We combined the background-subtracted X-ray image with a temperature map, built assuming the mean temperature value in each component (Table 1) within R_{500} and zero outside, to produce a pseudo-pressure map, that we smoothed with a Gaussian filter of 10′ FWHM to mimic the resolution of *Planck* *y*-maps. *Planck* cannot spatially resolve the three components of this object, therefore we expect the peak of the pseudo-pressure map to be located around the barycentre of the system, just because of resolution effects. The results are shown in Fig. 8, compared with the MILCA *y*-map. The position of the peak in the SZ map does not coincide with the peak of the pseudo pressure map: while the latter is located as expected at the barycentre between the three components, the *y*-map suggests an excess of pressure to the SW of component *A*. The offset between the two peaks is $\simeq 5'$.

We have performed some tests both on the X-ray and on the SZ maps to investigate the origin of this offset. On the X-ray side, we have produced surface brightness images using a different background modelling. The first test concerns the background subtraction: we used the ESAS software[7] to produce particle background and residual soft proton images and we created images of the "sky background" components (CXB and Galactic foregrounds), modelling them in an external annulus (Leccardi & Molendi 2008) and rescaling them across the field of view (Ettori et al. 2010). Point sources could also affect the position of the pseudo pressure peak, therefore

[6] Although deriving pseudo-pressure maps as discussed in the text is customary in the literature, we underline here that this approach is not completely valid. The X-ray surface brightness, ignoring the temperature dependance, is proportional to $\int n^2 dl$ and its square root is never equal to $\int n dl$, which is the expression that should enter in the definition of the Comptonisation parameter *y*. However, pseudo-pressure maps can still be used for qualitative comparison with the *y*-maps.

[7] http://heasarc.nasa.gov/docs/xmm/xmmhp_xmmesas.html

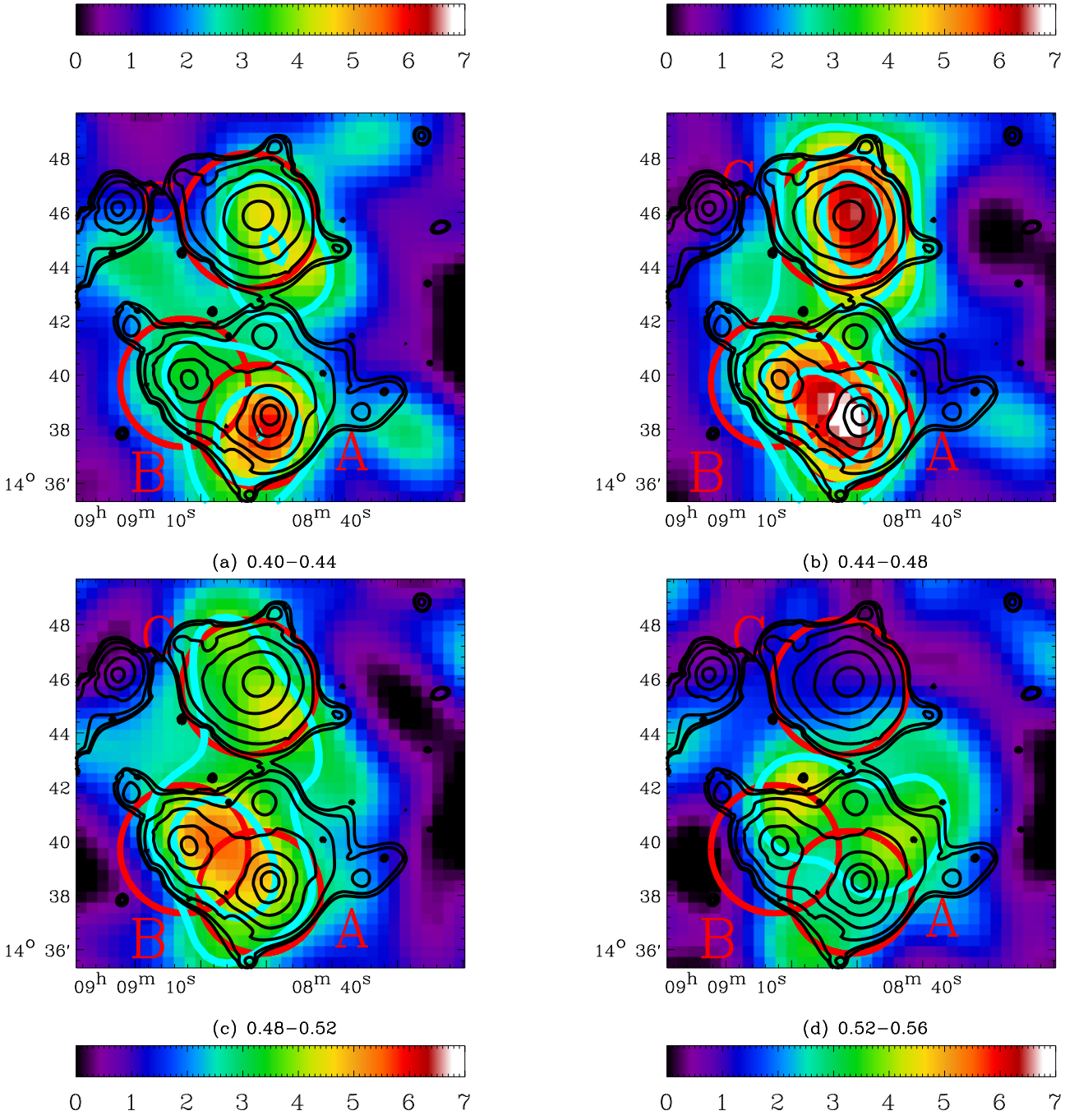

Fig. 7. Galaxy density maps for cluster members in the SDSS catalogue (colours) in different photometric redshift cuts: 0.40–0.44 (*upper left*); 0.44–0.48 (*upper right*); 0.48–0.52 (*lower left*); and 0.52–0.56 (*lower right*). The cyan contours overlaid mark the significance of each density peak at 3, 4, and 5σ, respectively. The black contours show the X-ray distribution and the red circles and letters mark the three components.

we ran a different point source algorithm using the SAS task `edetect_chain` on MOS and pn images in five energy bands, and we added undetected sources we identified with a visual inspection of the images. Both these tests showed a negligible impact on the position of the peak, which in fact is located where it is expected to be, at the barycentre of the three components.

For the SZ effect, we have compared the maps reconstructed with different ILC-based algorithms. Besides MILCA, we tested GMCA (Bobin et al. 2008) and NILC (Delabrouille et al. 2009) algorithms (see Planck Collaboration 2013, for a summary description and a comparison at the cluster scale of the three methods). The three y-maps are very consistent and the position of the peak does not change across the maps.

We also compared y-maps obtained with different releases of the data finding $\simeq 5'$ discrepancies in the position of the peak, comparable to the offset between the X-ray and y-maps peaks, discussed above. Indeed the y-map presented in Paper I showed a qualitative agreement with X-ray contours. We performed dedicated Monte Carlo simulations to estimate the expected error in the reconstruction of the position of PLCKG214.6+37.0. The presence of correlated noise in the y-map produced from *Planck* data can be a major source of error in reconstructing the position of clusters, in particular in the case of low signal

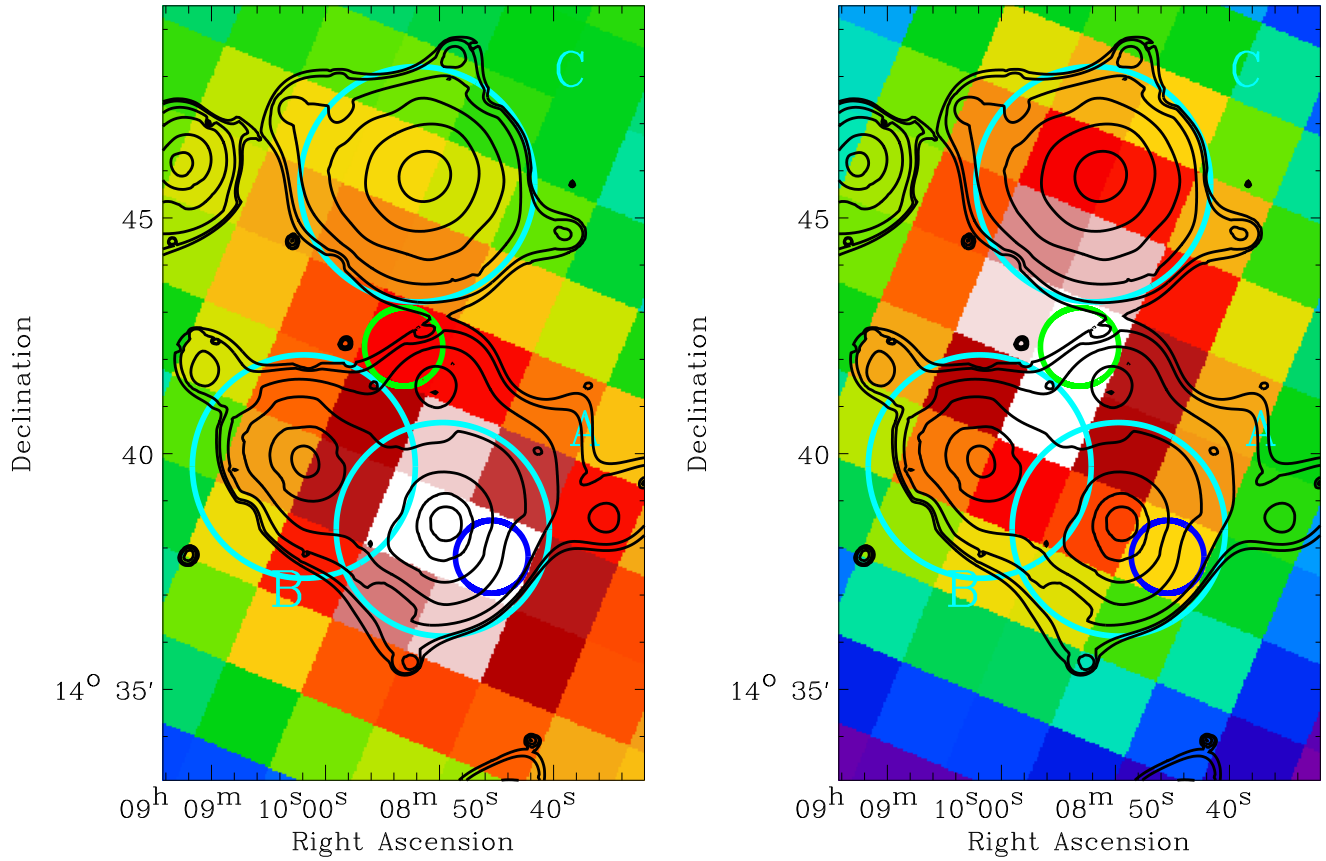

Fig. 8. MILCA *y*-map (*left panel*) compared with the pseudo pressure X-ray map degraded to the *y*-map resolution (*right panel*). X-ray contours and cyan circles indicating the three components are over-plotted to guide the eye. The green and blue circles mark the positions of the peaks in the *y*-map and in the pseudo-pressure distribution, respectively.

to noise systems such as PLCKG214.6+37.0. We first estimated the noise covariance matrix on the *Planck* Comptonisation parameter map of this system and produced 500 realisations of noise, to each of which we added the expected thermal SZ effect from PLCKG214.6+37.0 to construct mock *y*-maps. Then, we estimated the position of the supercluster in each of these maps. Finally, we computed the average and the standard deviation of the error on the reconstructed position and we obtained an average error of (4.5 ± 2.5) arcmin. Therefore, the offset between the reconstructed positions from the *Planck* *y*-map and the pseudo-pressure X-ray derived map of PLCKG214.6+37.0 is consistent with being due to noise. The same applies for the separation between the peak in the *Planck* *y*-map we show here and the one that was shown in Paper I.

6. Discussion and conclusion

The first observations of the multi-wavelength follow-up campaign of PLCKG214.6+37.0, a triple system of galaxy clusters discovered by *Planck*, have allowed us to improve our understanding of this object. With the new *XMM-Newton* observation we estimated the global properties of each component: the ICM temperatures range from 3.5 to 5 keV and the total masses within R_{500} are in the range $(2.2–3) \times 10^{14}\ M_{\odot}$. We detected the iron K$\alpha$ lines in the X-ray spectra of each component, and therefore we were able to confirm that components *A* and *C* are lying at the same redshift ($z = 0.45$). However, given the large angular separation of these two components (7.5′, corresponding to 2.6 Mpc, in the plane of the sky), they are likely undergoing a very early stage of interaction and we did not detect significant excess X-ray emission between these two components. For component *B*, we estimated a higher redshift from X-ray spectroscopy ($z = 0.48$), although consistent at 2σ with the best fit value for component *A*. A similar indication is supported by the optical data, with the photometric redshifts we retrieved from SDSS DR8. However, given the large uncertainties of our redshift estimates (based both on X-rays and on photometry), a more detailed picture of the three-dimensional structure of PLCKG214.6+37.0 will only be possible with the measurement of spectroscopic redshifts for a large sample of member galaxies, which is already foreseen with VLT in our follow-up programme.

Our redshift results are consistent with the three clusters being part of the same supercluster structure, which will eventually lead to the formation of a more massive object ($\simeq 10^{15}\ M_{\odot}$). This is also supported by our analysis of the galaxy population with SDSS data: the galaxy density maps show the presence of a possible population of inter-cluster galaxies, significant at 3σ, connecting the whole system (Fig. 7). However, the relaxed appearance of component *A*, its large distance (2.5 Mpc) in the plane of the sky from component *C* and along the line of sight from component *B*, as well as the absence of any detectable excess X-ray emission between the components, may suggest that we are witnessing a very early phase of interaction.

Using the X-ray results from the new *XMM-Newton* observation, we built a multi-component model that we used to extract

the total SZ signal from *Planck* data. We compared the improved estimate of Y_{SZ} with the prediction from X-rays and we found the latter to be about 68% of the measured SZ signal. The discrepancy between these two values is reduced with respect to Paper I and is not at the 1.2σ level.

The results from our simulations have shown that an offset as large as $5'$ can be expected in the reconstructed y-maps for low-significance objects, due to noise fluctuations and astrophysical contributions. With this study we have illustrated the expected difficulty of accurately reconstructing the two-dimensional SZ signal for objects with low signal-to-noise ratio. Indeed the instrumental noise and astrophysical contamination compete with the SZ effect at the detection limit threshold. Nonetheless, objects like PLCKG214.6+37.0 can be detected with a dedicated optimal filtering detection method, and the SZ signal can be reconstructed assuming priors (such as position, size, and relative intensity) from other wavelengths.

Despite a deep re-observation of this system with *XMM-Newton*, the intrinsic limitations of our X-ray data and of the current *Planck* SZ maps do not allow us, for the time being to assess the presence of possible inter-cluster emission.

A careful analysis of the galaxy dynamics in the complex potential of this object and of the mass distribution from weak lensing will both be available with our on-going optical follow up programme. These observations, combined with the results presented in this paper and with new *Planck* data obtained in two other full surveys of the sky, might lead to a deeper understanding of this triple system.

Acknowledgements. A description of the Planck Collaboration and a list of its members, indicating which technical or scientific activities they have been involved in, can be found at http://www.rssd.esa.int/Planck. The Planck Collaboration acknowledges the support of: ESA; CNES and CNRS/INSU-IN2P3-INP (France); ASI, CNR, and INAF (Italy); NASA and DoE (USA); STFC and UKSA (UK); CSIC, MICINN, and JA (Spain); Tekes, AoF, and CSC (Finland); DLR and MPG (Germany); CSA (Canada); DTU Space (Denmark); SER/SSO (Switzerland); RCN (Norway); SFI (Ireland); FCT/MCTES (Portugal); and DEISA (EU). The present paper is also partly based on observations obtained with *XMM-Newton*, an ESA science mission with instruments and contributions directly funded by ESA Member States and the USA (NASA), and on data retrieved from SDSS-III. Funding for SDSS-III has been provided by the Alfred P. Sloan Foundation, the Participating Institutions, the National Science Foundation, and the U.S. Department of Energy Office of Science. The SDSS-III web site is http://www.sdss3.org/.

References

Abazajian, K. N., Adelman-McCarthy, J. K., Agüeros, M. A., et al. 2009, ApJS, 182, 543
Arnaud, M., Pratt, G. W., Piffaretti, R., et al. 2010, A&A, 517, A92
Bahcall, N. A. 1999, in Formation of Structure in the Universe, 135
Balucinska-Church, M., & McCammon, D. 1992, ApJ, 400, 699
Bardelli, S., Zucca, E., Zamorani, G., Vettolani, G., & Scaramella, R. 1998, MNRAS, 296, 599
Bersanelli, M., Mandolesi, N., Butler, R. C., et al. 2010, A&A, 520, A4
Bobin, J., Moudden, Y., Starck, J.-L., Fadili, J., & Aghanim, N. 2008, Stat. Methodol., 5, 307
Bourdin, H., & Mazzotta, P. 2008, A&A, 479, 307
Bourdin, H., Arnaud, M., Mazzotta, P., et al. 2011, A&A, 527, A21
Cavagnolo, K. W., Donahue, M., Voit, G. M., & Sun, M. 2009, ApJS, 182, 12
De Luca, A., & Molendi, S. 2004, A&A, 419, 837
Delabrouille, J., Cardoso, J.-F., Le Jeune, M., et al. 2009, A&A, 493, 835
Dickey, J. M., & Lockman, F. J. 1990, ARA&A, 28, 215
Eriksen, H. K., Banday, A. J., Górski, K. M., & Lilje, P. B. 2004, ApJ, 612, 633
Ettori, S., Gastaldello, F., Leccardi, A., et al. 2010, A&A, 524, A68
Giacintucci, S., Venturi, T., Brunetti, G., et al. 2005, A&A, 440, 867
Górski, K. M., Hivon, E., Banday, A. J., et al. 2005, ApJ, 622, 759
Grevesse, N., & Sauval, A. J. 1998, Space Sci. Rev., 85, 161
Hurier, G., Hildebrandt, S. R., & Macias-Perez, J. F. 2010 [arXiv:1007.1149]
Kravtsov, A. V., Vikhlinin, A., & Nagai, D. 2006, ApJ, 650, 128
Kull, A., & Böhringer, H. 1999, A&A, 341, 23
Kuntz, K. D., & Snowden, S. L. 2000, ApJ, 543, 195
Kuntz, K. D., & Snowden, S. L. 2008, A&A, 478, 575
Lamarre, J., Puget, J., Ade, P. A. R., et al. 2010, A&A, 520, A9
Leahy, J. P., Bersanelli, M., D'Arcangelo, O., et al. 2010, A&A, 520, A8
Leccardi, A., & Molendi, S. 2008, A&A, 487, 461
Liivamägi, L. J., Tempel, E., & Saar, E. 2012, A&A, 539, A80
Lumb, D. H., Warwick, R. S., Page, M., & De Luca, A. 2002, A&A, 389, 93
Mandolesi, N., Bersanelli, M., Butler, R. C., et al. 2010, A&A, 520, A3
Maurogordato, S., Sauvageot, J. L., Bourdin, H., et al. 2011, A&A, 525, A79
Melin, J., Bartlett, J. G., & Delabrouille, J. 2006, A&A, 459, 341
Menanteau, F., Hughes, J. P., Sifon, C., et al. 2012, ApJ, 748, 7
Mennella A., Butter, R. C., Curto, A., et al. 2011, A&A, 536, A3
Mroczkowski, T., Dicker, S., Sayers, J., et al. 2012, ApJ, 761, 47
Planck Collaboration 2011a, A&A, 536, A1
Planck Collaboration 2011b, A&A, 536, A2
Planck Collaboration 2011c, A&A, 536, A9
Planck Collaboration 2011d, A&A, 536, A8
Planck Collaboration 2011e, A&A, 536, A10
Planck Collaboration 2011f, A&A, 536, A26
Planck Collaboration 2013, A&A, 550, A131
Planck HFI Core Team 2011a, A&A, 536, A4
Planck HFI Core Team 2011b, A&A, 536, A6
Pratt, G. W., Croston, J. H., Arnaud, M., & Böhringer, H. 2009, A&A, 498, 361
Rosset, C., Tristram, M., Ponthieu, N., et al. 2010, A&A, 520, A13
Rossetti, M., Ghizzardi, S., Molendi, S., & Finoguenov, A. 2007, A&A, 463, 839
Sakelliou, I., & Ponman, T. J. 2004, MNRAS, 351, 1439
Slezak, E., Durret, F., & Gerbal, D. 1994, AJ, 108, 1996
Smith, R. K., Brickhouse, N. S., Liedahl, D. A., & Raymond, J. C. 2001, ApJ, 556, L91
Starck, J.-L., & Pierre, M. 1998, in Astronomical Data Analysis Software and Systems VII, eds. R. Albrecht, R. N. Hook, & H. A. Bushouse, ASP Conf. Ser., 145, 500
Starck, J. L., Fadili, J., & Murtagh, F. 2007, IEEE Trans. Image Process., 16
Sunyaev, R. A., & Zeldovich, Y. B. 1972, Comm. Astrophys. Space Phys., 4, 173
Tauber, J. A., Mandolesi, N., Puget, J., et al. 2010, A&A, 520, A1
Vikhlinin, A., Forman, W., & Jones, C. 1997, ApJ, 474, L7
Vikhlinin, A., Kravtsov, A., Forman, W., et al. 2006, ApJ, 640, 691
Zacchei, A., Maino, D., Baccigalupi, C. A., et al. 2011, A&A, 536, A5
Zhang, B., Fadili, J., & Starck, J. L. 2008, IEEE Trans. Image Process., 17

[1] APC, AstroParticule et Cosmologie, Université Paris Diderot, CNRS/IN2P3, CEA/lrfu, Observatoire de Paris, Sorbonne Paris Cité, 10 rue Alice Domon et Léonie Duquet, 75205 Paris Cedex 13, France
[2] Aalto University Metsähovi Radio Observatory, Metsähovintie 114, 02540 Kylmälä, Finland
[3] Academy of Sciences of Tatarstan, Bauman Str., 20, 420111 Kazan, Republic of Tatarstan, Russia
[4] African Institute for Mathematical Sciences, 6-8 Melrose Road, Muizenberg, Cape Town, South Africa
[5] Agenzia Spaziale Italiana Science Data Center, c/o ESRIN, via Galileo Galilei, Frascati, Italy
[6] Agenzia Spaziale Italiana, Viale Liegi 26, Roma, Italy
[7] Astrophysics Group, Cavendish Laboratory, University of Cambridge, J J Thomson Avenue, Cambridge CB3 0HE, UK
[8] Atacama Large Millimeter/submillimeter Array, ALMA Santiago Central Offices, Alonso de Cordova 3107, Vitacura, 763 0355 Casilla, Santiago, Chile
[9] CITA, University of Toronto, 60 St. George St., Toronto ON M5S 3H8, Canada
[10] CNRS, IRAP, 9 Av. Colonel Roche, BP 44346, 31028 Toulouse Cedex 4, France
[11] California Institute of Technology, Pasadena, California, USA
[12] Centre of Mathematics for Applications, University of Oslo, Blindern, Oslo, Norway
[13] Centro de Astrofísica, Universidade do Porto, Rua das Estrelas, 4150-762 Porto, Portugal
[14] Centro de Estudios de Física del Cosmos de Aragón (CEFCA), Plaza San Juan, 1, planta 2, 44001 Teruel, Spain
[15] Computational Cosmology Center, Lawrence Berkeley National Laboratory, Berkeley, California, USA

[16] Consejo Superior de Investigaciones Científicas (CSIC), Madrid, Spain
[17] DSM/Irfu/SPP, CEA-Saclay, 91191 Gif-sur-Yvette Cedex, France
[18] DTU Space, National Space Institute, Technical University of Denmark, Elektrovej 327, 2800 Kgs. Lyngby, Denmark
[19] Département de Physique Théorique, Université de Genève, 24 Quai E. Ansermet, 1211 Genève 4, Switzerland
[20] Departamento de Física Fundamental, Facultad de Ciencias, Universidad de Salamanca, 37008 Salamanca, Spain
[21] Departamento de Física, Universidad de Oviedo, Avda. Calvo Sotelo s/n, Oviedo, Spain
[22] Department of Astronomy and Geodesy, Kazan Federal University, Kremlevskaya Str., 18, 420008 Kazan, Russia
[23] Department of Astrophysics/IMAPP, Radboud University Nijmegen, PO Box 9010, 6500 GL Nijmegen, The Netherlands
[24] Department of Physics & Astronomy, University of British Columbia, 6224 Agricultural Road, Vancouver, British Columbia, Canada
[25] Department of Physics and Astronomy, Dana and David Dornsife College of Letter, Arts and Sciences, University of Southern California, Los Angeles, CA 90089, USA
[26] Department of Physics, Gustaf Hällströmin katu 2a, University of Helsinki, Helsinki, Finland
[27] Department of Physics, Princeton University, Princeton, New Jersey, USA
[28] Department of Physics, University of California, Berkeley, California, USA
[29] Department of Physics, University of California, One Shields Avenue, Davis, California, USA
[30] Department of Physics, University of California, Santa Barbara, California, USA
[31] Department of Physics, University of Illinois at Urbana-Champaign, 1110 West Green Street, Urbana, Illinois, USA
[32] Department of Statistics, Purdue University, 250 N. University Street, West Lafayette, Indiana, USA
[33] Dipartimento di Fisica e Astronomia G. Galilei, Università degli Studi di Padova, via Marzolo 8, 35131 Padova, Italy
[34] Dipartimento di Fisica e Scienze della Terra, Università di Ferrara, via Saragat 1, 44122 Ferrara, Italy
[35] Dipartimento di Fisica, Università La Sapienza, P. le A. Moro 2, Roma, Italy
[36] Dipartimento di Fisica, Università degli Studi di Milano, via Celoria, 16 Milano, Italy
[37] Dipartimento di Fisica, Università degli Studi di Trieste, via A. Valerio 2, Trieste, Italy
[38] Dipartimento di Fisica, Università di Roma Tor Vergata, via della Ricerca Scientifica, 1, Roma, Italy
[39] Dipartimento di Matematica, Università di Roma Tor Vergata, via della Ricerca Scientifica, 1, Roma, Italy
[40] Discovery Center, Niels Bohr Institute, Blegdamsvej 17, Copenhagen, Denmark
[41] Dpto. Astrofísica, Universidad de La Laguna (ULL), 38206 La Laguna, Tenerife, Spain
[42] European Southern Observatory, ESO Vitacura, Alonso de Cordova 3107, Vitacura, 19001 Casilla, Santiago, Chile
[43] European Space Agency, ESAC, Planck Science Office, Camino bajo del Castillo, s/n, Urbanización Villafranca del Castillo, Villanueva de la Cañada, Madrid, Spain
[44] European Space Agency, ESTEC, Keplerlaan 1, 2201 AZ Noordwijk, The Netherlands
[45] GEPI, Observatoire de Paris, Section de Meudon, 5 place J. Janssen, 92195 Meudon Cedex, France
[46] Helsinki Institute of Physics, Gustaf Hällströmin katu 2, University of Helsinki, Helsinki, Finland
[47] INAF – Osservatorio Astronomico di Padova, Vicolo dell'Osservatorio 5, Padova, Italy
[48] INAF – Osservatorio Astronomico di Roma, via di Frascati 33, Monte Porzio Catone, Italy
[49] INAF – Osservatorio Astronomico di Trieste, via G.B. Tiepolo 11, Trieste, Italy
[50] INAF Istituto di Radioastronomia, via P. Gobetti 101, 40129 Bologna, Italy
[51] INAF/IASF Bologna, via Gobetti 101, Bologna, Italy
[52] INAF/IASF Milano, via E. Bassini 15, Milano, Italy
[53] INFN, Sezione di Roma 1, Universit'a di Roma Sapienza, Piazzale Aldo Moro 2, 00185 Roma, Italy
[54] IPAG: Institut de Planétologie et d'Astrophysique de Grenoble, Université Joseph Fourier, Grenoble 1/CNRS-INSU, UMR 5274, 38041 Grenoble, France
[55] IUCAA, Post Bag 4, Ganeshkhind, Pune University Campus, Pune 411 007, India
[56] Imperial College London, Astrophysics group, Blackett Laboratory, Prince Consort Road, London, SW7 2AZ, UK
[57] Infrared Processing and Analysis Center, California Institute of Technology, Pasadena, CA 91125, USA
[58] Institut Néel, CNRS, Université Joseph Fourier Grenoble I, 25 rue des Martyrs, Grenoble, France
[59] Institut Universitaire de France, 103, bd Saint-Michel, 75005, Paris, France
[60] Institut d'Astrophysique Spatiale, CNRS (UMR 8617), Université Paris-Sud 11, Bâtiment 121, Orsay, France
[61] Institut d'Astrophysique de Paris, CNRS (UMR 7095), 98bis boulevard Arago, 75014, Paris, France
[62] Institute for Space Sciences, Bucharest-Magurale, Romania
[63] Institute of Astro and Particle Physics, Technikerstrasse 25/8, University of Innsbruck, 6020, Innsbruck, Austria
[64] Institute of Astronomy and Astrophysics, Academia Sinica, Taipei, Taiwan
[65] Institute of Astronomy, University of Cambridge, Madingley Road, Cambridge CB3 0HA, UK
[66] Institute of Theoretical Astrophysics, University of Oslo, Blindern, Oslo, Norway
[67] Instituto de Astrofísica de Canarias, C/Vía Láctea s/n, La Laguna, Tenerife, Spain
[68] Instituto de Física de Cantabria (CSIC-Universidad de Cantabria), Avda. de los Castros s/n, Santander, Spain
[69] Jet Propulsion Laboratory, California Institute of Technology, 4800 Oak Grove Drive, Pasadena, California, USA
[70] Jodrell Bank Centre for Astrophysics, Alan Turing Building, School of Physics and Astronomy, The University of Manchester, Oxford Road, Manchester, M13 9PL, UK
[71] Kapteyn Astronomical Institute, University of Groningen, Landleven 12, 9747 AD Groningen, The Netherlands
[72] Kavli Institute for Cosmology Cambridge, Madingley Road, Cambridge, CB3 0HA, UK
[73] LAL, Université Paris-Sud, CNRS/IN2P3, Orsay, France
[74] LERMA, CNRS, Observatoire de Paris, 61 avenue de l'Observatoire, Paris, France
[75] Laboratoire AIM, IRFU/Service d'Astrophysique – CEA/DSM – CNRS – Université Paris Diderot, Bât. 709, CEA-Saclay, 91191 Gif-sur-Yvette Cedex, France
[76] Laboratoire Traitement et Communication de l'Information, CNRS (UMR 5141) and Télécom ParisTech, 46 rue Barrault, 75634 Paris Cedex 13, France
[77] Laboratoire de Physique Subatomique et de Cosmologie, Université Joseph Fourier Grenoble I, CNRS/IN2P3, Institut National Polytechnique de Grenoble, 53 rue des Martyrs, 38026 Grenoble Cedex, France
[78] Laboratoire de Physique Théorique, Université Paris-Sud 11 & CNRS, Bâtiment 210, 91405 Orsay, France
[79] Lawrence Berkeley National Laboratory, Berkeley, California, USA
[80] Max-Planck-Institut für Astrophysik, Karl-Schwarzschild-Str. 1, 85741 Garching, Germany
[81] Max-Planck-Institut für Extraterrestrische Physik, Giessenbachstraße, 85748 Garching, Germany
[82] MilliLab, VTT Technical Research Centre of Finland, Tietotie 3, Espoo, Finland
[83] National University of Ireland, Department of Experimental Physics, Maynooth, Co. Kildare, Ireland
[84] Niels Bohr Institute, Blegdamsvej 17, Copenhagen, Denmark

[85] Observational Cosmology, Mail Stop 367-17, California Institute of Technology, Pasadena, CA, 91125, USA
[86] Optical Science Laboratory, University College London, Gower Street, London, UK
[87] SISSA, Astrophysics Sector, via Bonomea 265, 34136 Trieste, Italy
[88] School of Physics and Astronomy, Cardiff University, Queens Buildings, The Parade, Cardiff, CF24 3AA, UK
[89] Space Research Institute (IKI), Profsoyuznaya 84/32, Moscow, Russia
[90] Space Research Institute (IKI), Russian Academy of Sciences, Profsoyuznaya Str, 84/32, 117997 Moscow, Russia
[91] Space Sciences Laboratory, University of California, Berkeley, California, USA
[92] Stanford University, Dept of Physics, Varian Physics Bldg, 382 via Pueblo Mall, Stanford, California, USA
[93] TÜBİTAK National Observatory, Akdeniz University Campus, 07058, Antalya, Turkey
[94] Tuorla Observatory, Department of Physics and Astronomy, University of Turku, Väisäläntie 20, 21500 Piikkiö, Finland
[95] UPMC Univ Paris 06, UMR7095, 98bis boulevard Arago, 75014, Paris, France
[96] Université Denis Diderot (Paris 7), 75205 Paris Cedex 13, France
[97] Université de Toulouse, UPS-OMP, IRAP, 31028 Toulouse Cedex 4, France
[98] University Observatory, Ludwig Maximilian University of Munich, Scheinerstrasse 1, 81679 Munich, Germany
[99] University of Granada, Departamento de Física Teórica y del Cosmos, Facultad de Ciencias, Granada, Spain
[100] Warsaw University Observatory, Aleje Ujazdowskie 4, 00-478 Warszawa, Poland